



Minerva Access is the Institutional Repository of The University of Melbourne

Author/s:

Wen, D;Meng, J;Cadusch, JJ;Crozier, KB

Title:

VCSELs with On-Facet Metasurfaces for Polarization State Generation and Detection

Date:

2021-05-01

Citation:

Wen, D., Meng, J., Cadusch, J. J. & Crozier, K. B. (2021). VCSELs with On-Facet Metasurfaces for Polarization State Generation and Detection. *Advanced Optical Materials*, 9 (9), <https://doi.org/10.1002/adom.202001780>.

Persistent Link:

<https://hdl.handle.net/11343/294850>

VCSELs with On-Facet Metasurfaces for Polarization State Generation and Detection

*Dandan Wen, Jiajun Meng, Jasper J. Cadusch, and Kenneth B. Crozier**

Dr. D. Wen, Mr. J. Meng, Dr. J. J. Cadusch
Department of Electrical and Electronic Engineering, University of Melbourne, Victoria
3010, Australia

Prof. K. B. Crozier
School of Physics, University of Melbourne, Victoria 3010, Australia
Department of Electrical and Electronic Engineering, University of Melbourne, Victoria
3010, Australia
Australian Research Council (ARC) Centre of Excellence for Transformative Meta-Optical
Systems, University of Melbourne, Victoria 3010, Australia

E-mail: kcrozier@unimelb.edu.au

Keywords: VCSEL, metasurface, polarization generation, polarization detection

Abstract: Polarization plays a critical role in optical systems that range from optical communications to imaging, lithography, metrology and data storage. Thus, in systems that need to generate a certain polarization state, a light source (e.g. laser) is combined with polarization control elements such as polarizers, polarizing beam-splitters and waveplates. Similarly, in systems requiring polarization state detection, such elements are combined with photodetectors. There is currently a trend however toward miniaturized optical systems. This motivates the question of how to achieve what may be argued as an ultimate level of miniaturization: a single chip that can both generate light with a prescribed polarization state and detect the polarization state of light impinging upon it. Here, we demonstrate this via vertical cavity surface emitting lasers (VCSELs) with on-facet metasurfaces. Two classes of devices are demonstrated. The first class employs high index dielectric metasurfaces (amorphous silicon nanofins), while the second class uses plasmonic metasurfaces (aluminum bilayer gratings). Each can operate as a laser (to generate) and as a photodetector (to detect) circularly or linearly polarized light.

1. Introduction

Vertical cavity emitting lasers (VCSELs) have attracted much attention in recent years due to their low cost, their ability to be fabricated in arrays without excessive complexity, and the fact that they can be readily integrated with other systems^[1]. VCSELs have thus been employed in a variety of applications including optical fiber communications^[2], frequency combs^[3], computer mice, and face identification^[4]. For some important applications like VCSEL-based data communication and optical sensing, a stable polarization is beneficial or even necessary^[5]. However, VCSELs generally do not emit in a single polarization state for the following reasons. First, the beam in a VCSEL cavity travels perpendicular to the gain area, so that the electric field of different polarization modes is parallel to the gain area. Different modes thus generally have about the same gain. Second, the distributed Bragg reflectors (DBRs) are not polarization-dependent^[6]. Third, because VCSELs do not have an inherent mechanism for polarization stabilization, fabrication inconsistency or a small change in operating conditions^[7] may cause the polarization instability. For example, when the drive current is high enough, lasing can occur on a higher order transverse mode (and not just on the fundamental mode). The polarization of the higher order mode tends to be perpendicular to the fundamental mode^[8]. Birefringence and linear dichroism in the VCSEL cavity also affect the output polarization states. The former is caused by the electro-optic and elasto-optic effects^[9], and the latter refers to the gain difference between two polarization modes induced by the slight dependence of the complex refractive index of the medium with wavelength and polarization. To achieve a stable polarization output, much research has been done. This can be generally categorized into the following approaches: polarization-dependent gain^[10]/or mirrors^[11], asymmetric resonators^[12], and external optical feedback^[13].

Inspired by the various methods that have been employed for output polarization control, we also arrive at the following question. Thinking in reverse, can a VCSEL detect the polarization state of light illuminating it? Little has been reported on this point. This is because the polarization control methods mentioned above are based on differentiating the lasing conditions of the orthogonal polarization modes, i.e. suppressing one while allowing the other to lase. The intentionally introduced difference is often weak^[6]. This is acceptable for laser operation, but unsuitable if the device is to be operated as a photodetector for polarization state detection, i.e. it can hardly distinguish between orthogonal polarization states. Here, we demonstrate a different approach to VCSELs with controlled output polarization. Our approach furthermore allows the same device to be operated as a photodetector that can distinguish between beams with different polarization states that illuminate it. We demonstrate two types of devices. In the first, we fabricate an amorphous silicon (a-Si) metasurface on the VCSEL facet (**Figure 1a**) to realize a multifunctional device. When the VCSEL is forward biased, it operates as a laser and produces left- and right- handed circularly polarized (LCP and RCP) beams that propagate in different directions. When the VCSEL is reverse biased, it operates as a photodetector and can distinguish the helicity of the light incident upon it (at oblique incidence). Our second device is a VCSEL with an aluminum bilayer grating metasurface (**Figure 1b**) on its facet. Forward bias results in laser operation and a linearly polarized output beam. When reverse biased, it works as a polarization-selective photodetector.

We consider the polarization generation and detection functions of a single VCSEL since the device may benefit optical communication systems, in particular free-space optical interconnects. These offer promising solutions to achieve high bandwidth, low-power-consumption data communication links^[14]. In high density optical interconnect applications, it is often advantageous to integrate monolithically the optical source and photodetector on the same substrate^[15]. As each device we demonstrate functions as both source and detector, we

achieve this, with the integrated metasurfaces adding the functionalities of stable output polarization and polarization-selective detection. One might expect that the source and photodetector would need to be of different designs. For example, Louderback et al^[16] fabricate two types of VCSELs on the same substrate. Those with oxidized AIAs layers in bottom distributed Bragg reflector (DBR) work as light emitters while those for which the AIAs are not oxidized work as detectors. Similarly, Ortiz et al^[15] demonstrate a chip with two types of VCSELs. Some operate as emitters while others are detectors. The two classes of devices have different numbers of top DBRs. We show that it is not necessary to use different fabrication approaches for the lasers and detectors (e.g. those used by Louderback et al^[16] and Ortiz et al^[15]),. A free space optical communications system based on our devices could also be readily reconfigured, i.e. the function (laser or detector) that a given device performs could be modified as needed.

We note that the splitting of RCP and LCP beams by metasurfaces have been demonstrated in previous works ^[17]. However, the integration of such metasurfaces with VCSELs has not been reported before to the best of our knowledge. The integration of plasmonic polarizers on light sources has also been shown ^[11c, 18], but these polarizers were not used for polarization state generation and detection simultaneously. The use of metasurfaces to control the wavefronts of the beams produced by VCSELs is also a topic of recent investigations. Xie et al ^[19] integrate dielectric metasurfaces on the GaAs substrate of a VCSEL to achieve arbitrary control of laser beam profiles. The metasurface can produce laser beams with low divergence angles or shape the output to be a Bessel beam or a vortex beam. Sun et al^[20] and Li et al^[21] demonstrate the generation of vortex beams by integrating amorphous silicon metasurfaces^[20] and silicon nitride spiral phase plates^[21] on the emitting facets of VCSELs. Li et al^[22] demonstrate a VCSEL whose top mirror comprises a high contrast grating that acts as both a microelectromechanical tunable mirror and an output beam shaper. Seghilani et al^[23] use a

dielectric metasurface to introduce a weak anisotropy called “orbital birefringence”, which can directly generate Laguerre-Gauss modes with vortex phase. Here we show that devices consisting of metasurfaces integrated with VCSELs can not only generate light beams with stable polarization states, but also operate as polarization dependent photodetectors.

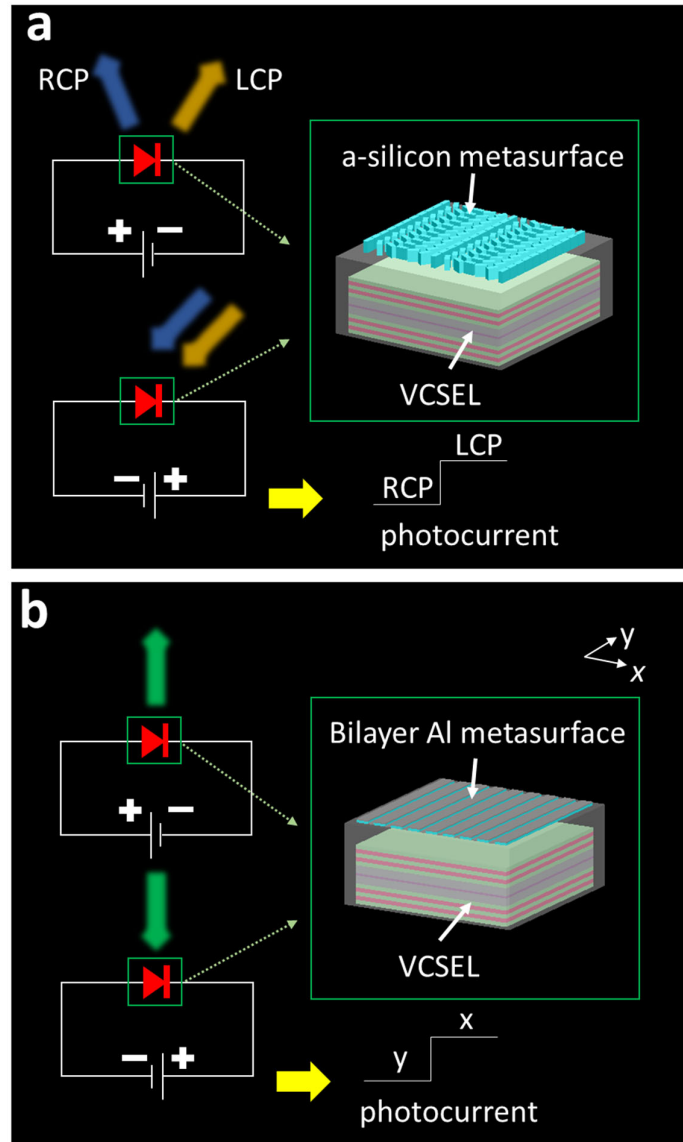


Figure 1. Schematic illustrations of devices and operating principles. (a) VCSEL with a-Si metasurface on top facet. Device can simultaneously generate RCP and LCP beams when operating as a laser (forward biased). Device can also distinguish helicity of incident light when

operated as a photodetector (reverse biased). (b) VCSEL with Al bilayer grating. Device generates an x -polarized beam (polarized perpendicular to the grating wires) when operating as a laser and distinguishes between x - and y - polarized incident light when operating as a photodetector.

2. Results

The VCSEL wafer we use has 34 pairs of n -doped DBRs as the high reflector and 24 pairs of p -doped DBRs as the output coupler, with the quantum wells in between (**Figure 2a**). Detailed structures of the DBRs and quantum wells can be found in Supplementary Note 1. VCSEL fabrication starts with the formation of a hollow square-shaped p -electrode on the cap layer (**Figure 2a**). This is achieved by the lift-off process with electron beam lithography (Vistec EPBG5000+), and electron beam evaporation (IntlVac NanoChrome II) of Ti (15 nm) and Au (100 nm). The hollow square has an outer side length of 12 μm and an inner side length of 8 μm . We next form an AZ4562 photoresist mask on the p -electrode using photolithography (Intelligent micropatterning SF100 XPRESS). We then perform inductively-coupled reactive ion etching (ICP-RIE, Oxford Instruments PlasmaLab 100, Ar: Cl₂=12sccm:4sccm) to form a mesa (**Figure 2b**). The AZ4562 mask is then removed with acetone. The use of a photoresist mask reduces the number of fabrication steps required in comparison to what would be needed were an SiO₂ mask used (Supplementary Note 2). The mesa has a depth of 4.27 μm . It thus goes through the top DBRs, the gain area, and stops at the fifth DBR pair below the gain area. After formation of the mesa, we spin coat SU8 onto the wafer to a thickness of 10 μm , i.e. the mesa is fully embedded in this layer. We then dry etch the SU8 (O₂: SF₆=50sccm:10sccm) to expose the p -electrode (**Figure 2c**). Since the structure is now planarized, we can make the contact line on top of the SU8 (**Figure 2d**). The wire connects the p -electrode to a large metallic pad (1 mm \times 1 mm, to be probed). We also sputter (Intlvac Nanochrome) AuGe (40nm-thick)

and Au (200nm-thick) on the backside of the VCSEL wafer as the n-electrode. Next, we spin coat another layer of SU8 (10 μm) to planarize the device (Figure 2e). This provides a platform onto which to fabricate the metasurface (Figure 2f). This means that SU8 is coated onto the device in two fabrication steps (Figure 2c and e) for planarization purposes. SU8 has favorable attributes for this function. It is almost transparent at the operating wavelength of our device (850 nm), meaning that light can be coupled in and out with high efficiency. It is also robust to most solvents when cured, including those used in the subsequent fabrication steps.

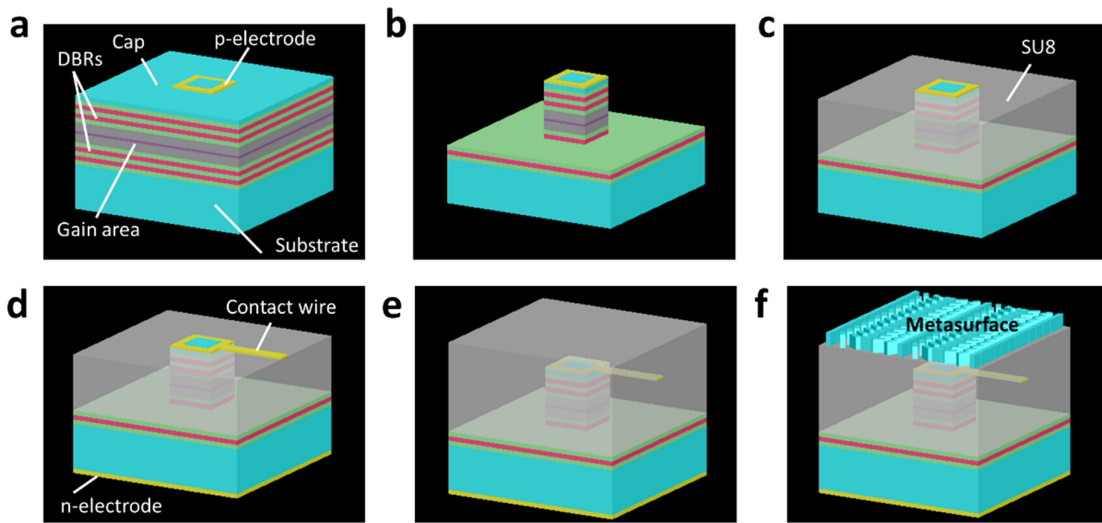


Figure 2. Fabrication process for metasurface-integrated VCSELs. (a) Formation of p-electrode on cap layer. (b) Square mesa with p-electrode on top. (c) SU8 planarization. SU8 is spin coated on chip, then etched back to expose p-electrode. (d) Contact wire and back electrode formation. (e) SU8 planarization. (f) Device after formation of metasurface on VCSEL.

Metasurfaces made from high refractive index dielectric materials usually have higher efficiency than their plasmonic counterparts^[24]. Here we choose amorphous silicon (a-Si) which has moderately low loss at 850 nm. We first deposit a-Si to a thickness of 600 nm on the SU8 using PECVD (Oxford Instruments PlasmaLab 100). We then define a hard mask

consisting of an array of Cr nano-rectangles on the a-Si through e-beam lithography, e-beam evaporation and lift-off. It is worth noting that the conductivity of the a-Si is weak and special steps are needed to perform e-beam lithography on it (Supplementary Note 3). We then perform ICP-RIE ($\text{SF}_6:\text{C}_4\text{F}_8=60\text{sccm}:90\text{sccm}$) to form the a-Si nanopillars that comprise this metasurface. We next remove the Cr nano-rectangles with Cr etchant. We fabricate the VCSELs in a 4×4 array, with the distance between VCSELs being $200 \mu\text{m}$. The VCSEL array thus occupies an area of approximately $600 \mu\text{m} \times 600 \mu\text{m}$. To ensure that it covers the VCSEL array, the a-Si metasurface is chosen to have an extent of $1 \text{mm} \times 1 \text{mm}$. As this metasurface contains a-Si nanopillars on a 300nm period, this comprises 3333×3333 pixels. For the bilayer grating metasurface, fabrication is simpler, comprising just one round of e-beam lithography and e-beam evaporation (Al, 60nm). The extent is also $1 \text{mm} \times 1 \text{mm}$. The grating period is 230nm , meaning that the metasurface contains 4348 periods.

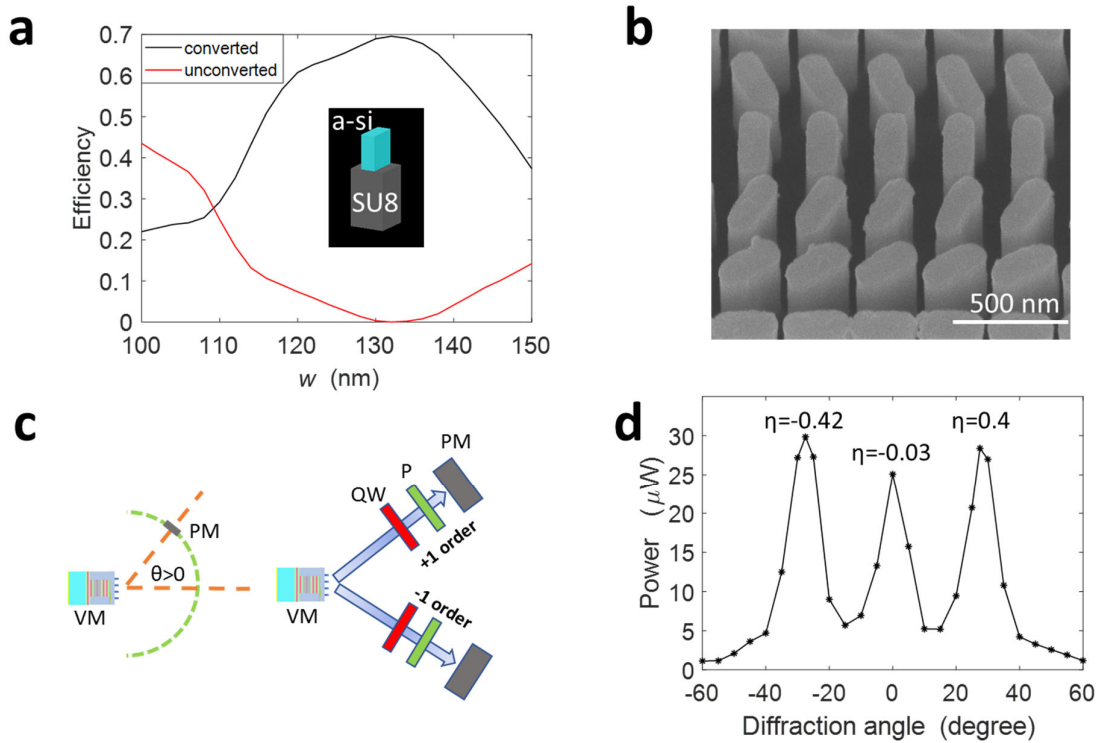


Figure 3. Generation of LCP and RCP laser beams from VCSEL with a-Si metasurface. (a) Simulated conversion efficiency of metasurface as a function of a-Si nanopillar width (w). A-

si nanopillars are arranged in a square lattice with 300 nm period. The nanopillars have heights and lengths of 600 nm and 280 nm, respectively. Refractive indices of a-Si and SU8 are taken as 3.707 and 1.57, respectively. (b) SEM image of a-Si metasurface on SU8. Viewing angle is 25°. Scale bar: 500 nm. (c) Left panel: schematic of set-up used to measure the power versus the diffraction angle. Right panel: schematic of set-up used to characterize polarization state of light output from device. VM: VCSEL with metasurface. QW: quarter wave plate. P: linear polarizer. PM: power meter. (d) Measured laser power versus the diffraction angle. Degree of circular polarization (DOCP, η) of the 0th and $\pm 1^{\text{st}}$ orders are measured and labelled in plot.

We next simulate the efficiency of our a-Si metasurface, which comprises a square array of a-Si nanopillars on SU8. A schematic of a single unit cell of the a-Si metasurface is included in the inset of **Figure 3a**. Under circularly polarized (CP) illumination, a portion of the transmitted light has a helicity opposite to that of the incident light and carries geometric phase^[17a, 25]. The ratio between the power of this (helicity-converted) portion and that of the CP illumination is defined as the conversion efficiency. For our e-beam lithography design file, we choose $w = 120$ nm and $l = 270$ to account for the fact that, in our experience, the dimensions of as-fabricated a-Si nanopillars are often larger than the dimensions of design files due to overexposure. A scanning electron microscope (SEM) image of the metasurface is shown in Figure 3b. The measured w and l are 124 nm and 280 nm, respectively. Neighboring nanopillars in the same line are rotated by 30°, which enables the metasurface to work as a polarization beam splitter^[17b]. When the light from the VCSEL passes through the metasurface, it provides different phase gradient to the LCP and RCP components of the incident light, which are deflected to -1st and +1st orders ($\pm 28.2^\circ$). As a result, the polarization states of the $\pm 1^{\text{st}}$ orders are not affected by the polarization of the incident light.

To verify this functionality, we first measure the power of the VCSEL as a function of diffraction angle. The VCSEL is operated with a current of 8.5 mA. The VCSEL is mounted on a three-axis translation stage and the voltage applied to it is provided by probe station probes. As shown in the left panel of Figure 3c, to measure the power as a function of diffraction angle, we translate a power meter along a semicircle that is centered on the VCSEL and has a radius of 6.2 cm. The measured power is shown in Figure 3d, confirming that most of the light is diffracted to the $\pm 1^{\text{st}}$ orders. The diffraction efficiency of the metasurface is defined as the total power of the 0^{th} and $\pm 1^{\text{st}}$ orders divided by the output power of the VCSEL before the integration of the metasurface. It is measured to be 53 %. Here, we use the degree of circular polarization (DOCP) to characterize these orders. This is defined as $\eta = (I_{\text{RCP}} - I_{\text{LCP}}) / (I_{\text{RCP}} + I_{\text{LCP}})$. I_{RCP} and I_{LCP} are the intensities of the RCP and LCP components in the beam to be characterized. The right panel of Figure 3c shows the setup for the measurement of η . The LCP and RCP component of the diffracted light can be determined by measuring the power, with the transmission direction of the polarizer and the fast axis direction of the quarter wave plate appropriately chosen. The measured values of η are indicated in Figure 3d. It can be seen that the $+1^{\text{st}}$ order and -1^{st} order have different helicity, i.e. η takes different signs. For RCP and LCP plane waves, η would take values of +1 and -1, respectively. We attribute the differences between measured and predicted values for DOCP as being largely due to fabrication imperfections. This is discussed further in Supplementary Note 4. In addition to the DOCP, we measure the Stokes parameters of the light output from the device. The results are shown in Table S1 in Supplementary Note 5.

We next consider the effect of the metasurface on the lasing characteristics. We note that we would expect that the addition of the a-Si metasurface to the VCSEL would result in part of the light (that would otherwise have been output from the VCSEL) being reflected back into the device and being coupled into the gain area. We conclude however, that this would have

minimal effect on lasing. For the a-Si metasurface used here, the reflection coefficient is low. In addition, not much of the light reflected from the a-Si metasurface reaches the gain area due to the resonator structure of the VCSEL. We measure the output spectrum and light-current (L-I) curve of a device before and after metasurface integration. The results (Supplementary Note 6) reveal that the wavelength of peak emission and the threshold current are not modified substantially.

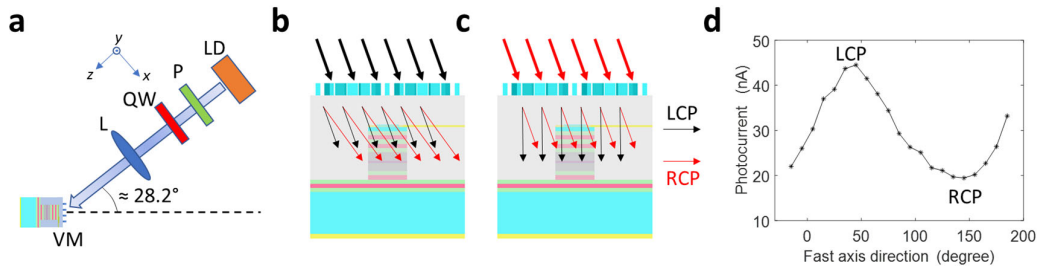


Figure 4. Helicity detection enabled by the VCSEL with a-Si metasurface. (a) Experimental setup used to verify helicity-distinguishing functionality. (b)-(c) Schematic of components of transmitted beam when incident light is LCP (b) and RCP (c). (d) Measured photocurrent versus fast axis direction of quarter wave plate when VCSEL is biased at -2 V.

We have thus far considered the operation of our VCSEL device with integrated a-Si metasurface as a light emitter. We next discuss its use as a light detector. I.e., when operated under reverse bias, the absorption of photons creates the electron-hole pairs that are separated by the junction potential and collected as photocurrent. Here we bias the VCSEL at -2 V, at which the dark current is less than 1 pA. **Figure 4a** shows the experimental setup to verify the helicity-distinguishing functionality of the VCSEL. Light from a laser diode module (Thorlabs CPS850) is incident on the device at an angle corresponding to the 1st diffraction order. The light first passes through a polarizer, whose transmission axis is along the y -direction. It then passes through a quarter waveplate. When the fast axis is at an angle of 45° with respect to the x -axis, the transmitted beam is LCP. Similarly, when it is -45° , the transmitted beam is RCP.

A lens ($f=6\text{cm}$) is used to loosely focus the beam onto the VCSEL. It is located at a distance of 7.0 cm from the VCSEL.

When the device operates as a laser (Figure 3), the LCP component of VCSEL beam is transformed by the metasurface and forms the 1st diffraction order (RCP). Based on the principle of reversibility of light, we expect that when an RCP beam is incident on the device at an angle corresponding to the 1st diffraction order, the converted component (LCP) will be normally-incident upon the VCSEL top DBR mirror. On the other hand, when the illuminating beam is LCP, the transmitted RCP light will be diverted away from the metasurface normal since it does not satisfy the condition for reversibility. This can be understood from the generalized law of refraction^[26]

$$\sin(\theta_t)n_t - \sin(\theta_i)n_i = \frac{\lambda_0}{2\pi} \frac{d\Phi}{dx} \quad (1)$$

The incident angle (θ_i) is equal to 28.2° . The refractive indices of air (n_i) and SU8 (n_t) are taken as 1 and 1.57, respectively. $d\Phi/dx$ represents the phase gradient provided to the converted part by the metasurface. In our design, we have $d\Phi/dx = 200^\circ \mu\text{m}^{-1}$ when the incident light is LCP, and the converted RCP beam is thus transmitted at an angle $\theta_t=37^\circ$. Similarly, we have $d\Phi/dx = -200^\circ \mu\text{m}^{-1}$ (i.e. the phase gradient is now opposite in sign) when the incident light is RCP, making the converted LCP transmitted at an angle of $\theta_t=0^\circ$. This is summarized schematically as Figure 4b: with LCP illumination (bold black arrow), the part of the transmitted beam that is unconverted (ie. still LCP, slim black arrow) propagates along the original direction, while the converted part (i.e. RCP, slim red arrow) is diverted further away from the VCSEL normal. We denote the contributions to photocurrent from the unconverted and converted parts as $I_{1\text{-uncv}}$ and $I_{1\text{-cv}}$, respectively. When the incident light is RCP (bold red arrow), the converted part (i.e. LCP, slim black arrow) is normally-incident on the VCSEL (Figure 4c). Similarly, we use $I_{2\text{-uncv}}$ and $I_{2\text{-cv}}$ to denote the contribution of the unconverted and converted parts in this case.

We next provide a physical interpretation for the observed differences in photocurrent with LCP and RCP illumination (Figure 4d). We first note that when the incident beam is LCP, it is of the same intensity as when it is RCP. It readily follows that $I_{1\text{-uncv}} = I_{2\text{-uncv}}$ since the unconverted LCP beam (with LCP illumination) will be coupled into the VCSEL with the same intensity and incident angle as the unconverted RCP beam (with RCP illumination). However, $I_{1\text{-cv}}$ and $I_{2\text{-cv}}$ are rather different for the following reasons. As shown in Figure 4c, when the illumination is RCP, the converted part (i.e. LCP) is normally incident on the top of the VCSEL. Only a tiny fraction of this part can reach the gain area, with most light being reflected by the top DBR stack (24 pairs). In addition, as discussed in further detail in the Supporting Information, a significant portion (~56%) of the incident light will be blocked by the top p-contact ring, which is of course not transparent at the wavelength under consideration (850 nm). We now consider LCP illumination. In this case (Figure 4b), the converted part (i.e. RCP) illuminates the VCSEL at an angle of 37° . This beam thus illuminates not only the top of the VCSEL, but also the mesa sidewall. The light striking the mesa sidewall does not encounter the full thickness (i.e. 24 pairs) of the top DBR. The fraction of the incident power that can reach the gain area is thus larger than the previous case in which the converted (LCP) beam is incident upon the top DBR stack at normal incidence. As a result, the photocurrent contribution from the converted (RCP) beam with LCP illumination ($I_{1\text{-cv}}$) is larger than that from the converted (LCP) beam with RCP illumination ($I_{2\text{-cv}}$). This is discussed in further detail in Supplementary Note 7. In Figure 4d, the measured photocurrent with varied illumination polarization (fast axis of quarter wave plate) is shown. The peak and the dip correspond to LCP and RCP illumination, respectively, which is consistent with the behavior we predicted. We next consider the responsivity of the detector to LCP illumination (at an angle of 37°). The optical power illuminating the detector is determined by characterizing the beam using the knife edge method. The beam from the laser diode module is elliptical, and we measure its full

width at half maximum (FWHM) along the major and minor axes to be $470\ \mu\text{m}$ and $120\ \mu\text{m}$, respectively. These are much larger than the gain area of the VCSEL ($12\ \mu\text{m}\times 12\ \mu\text{m}$). In the experiments, we adjust the position of laser spot to maximize the signal from the VCSEL (operating as a photodetector). In estimating the responsivity, we thus find the illumination power from the peak intensity. The latter is measured using the knife edge method to be $\sim 0.119\ \mu\text{W}/\mu\text{m}^2$. This illuminates the VCSEL at an angle of 37° . We thus estimate the power incident on the VCSEL by multiplying the peak intensity by the VCSEL area ($12\ \mu\text{m}\times 12\ \mu\text{m}$) and by the factor $\cos(37^\circ)$. The responsivity of the detector R is defined as the photocurrent divided by the incident power. The measured R has the value $3.24\ \text{mA}/\text{W}$ for the LCP light (incident at an angle of 37°).

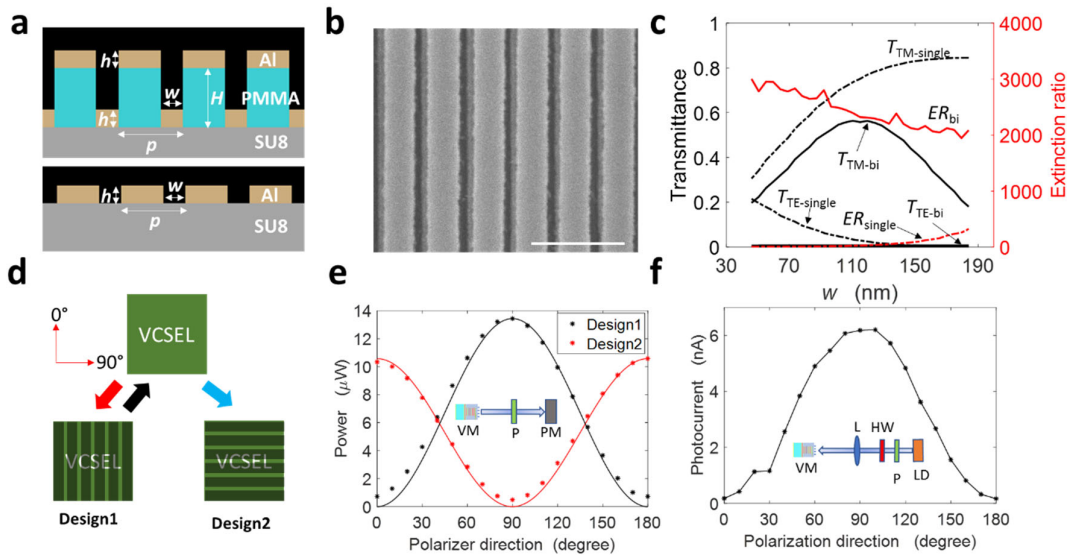


Figure 5. Linearly polarized light generation and detection by VCSEL with integrated bi-layer grating. (a) Schematic of bi-layer grating (top panel) and single layer grating (bottom panel). (b) SEM image of fabricated bi-layer grating. Scale bar: 500 nm. (c) Simulated transmittance of TM (TE) mode and extinction ratio. TM (TE) mode is defined to be light polarized perpendicular (parallel) to wires of grating. Extinction ratio is ratio between the transmittance of TM mode and TE mode. We have $h=60\ \text{nm}$, $p=230\ \text{nm}$ for both bi-layer and single layer gratings. Thickness of PMMA in bilayer grating (H) is 200 nm. Illumination is a plane wave

(wavelength 850 nm) impinging on metasurface from SU8 side at normal incidence. $T_{\text{TM-single}}$, $T_{\text{TE-single}}$, and ER_{single} represent TM, TE mode transmittance and extinction ratio of single layer grating. $T_{\text{TM-bi}}$, $T_{\text{TE-bi}}$, ER_{bi} represent corresponding parameters of bilayer grating. (d) Schematics of Design 1 and Design 2. (e) Inset: experimental setup used to determine polarization state of light output of our device. VCSEL is forward biased, with current of 3.13 mA. Power meter is 7 cm away from VCSEL. Asterisks: Measured power versus transmission direction of polarizer (angle between polarizer transmission direction and y -axis). Black curve: ideal $\sin^2(\theta)$ curve with the peak value set to be $13.43 \mu\text{W}$. Red curve: ideal $\cos^2(\theta)$ curve with the peak value set to be $10.57 \mu\text{W}$. (f) Inset: experimental setup used to characterize the VCSEL when operating as a detector (biased at -2V). Lens ($f=6\text{mm}$) is ~ 7.3 cm from VCSEL. HW: half-wave plate. Curve: measured photocurrent versus polarization direction of input light (linearly polarized).

To generate and detect the linearly polarized light with the same device, we need to integrate a polarizer with high extinction ratio (ER) and transmittance (T) with the VCSEL. Here we choose a bilayer grating^[27] for this purpose. This design is shown in **Figure 5a** (top panel) and b. It can be regarded as a three-layer structure: two wire-grid polarizers separated by a small distance. The light that passes through the first polarizer is partially reflected by the second one, then oscillates between the two layers. It thus functions like a Fabry-Perot cavity. To verify the FP interferometer-like property of the bilayer grating, we calculate the transmittance and reflectance of the three layers. We use these parameters in a multibeam interference model^[28], and find that the results agree well with our FDTD results (Supplementary Note 8). Our design goal is to achieve high extinction ratio and high transmittance. We fabricate a series of bilayer gratings on a glass substrate. We measure the extinction ratio of the fabricated samples and choose the best design for VCSEL integration (Supplementary Note 8). We also compare the

performance of the single layer grating and bilayer grating (Figure 5c). Although the single layer grating has higher T , its ER is much lower than the bilayer one. Here, we choose the bilayer grating with 230 nm period and 80 nm groove width, in anticipation of the groove width of fabricated sample being likely to be larger than the design.

A bilayer grating with wires along the 0° direction (Figure 5d), which corresponds to the $[1\ 1\ 0]$ crystal axis of the VCSEL, is first integrated on the VCSEL to form Design 1. We then insert a polarizer between the VCSEL and the power meter (Figure 5e, inset) to study the polarization direction of the output beam. The data we obtain when we measure power as a function of the polarizer direction (black symbols, Figure 5e) has a $\sin^2\theta$ dependence, indicating that the light output from our device is polarized along 90° . We next remove the grating by Al etchant (MicroChemicals GmbH), then fabricate a new grating whose wires are along the 90° -direction (i.e. along the $[1\ \bar{1}\ 0]$ crystal axis). This forms Design 2 (Figure 5d). We repeat the polarization measurement, with the resultant data points having a $\cos^2\theta$ dependence (red symbols, Figure 5e), indicating that the light is 0° - polarized. The results of Figure 5e verify that the output polarization is solely determined by the orientation of the grating wires. The measured extinction ratio is not as high as the simulation. This might be due to fabrication imperfections such as line edge roughness, misalignment of wire directions with the VCSEL crystal axis and oxidation of the aluminum. Nonetheless, the extinction ratio of our device is comparable to VCSELs that employ other methods for polarization stabilization^[29]. The spectra and the L-I curves of the VCSEL measured before and after integration with the bilayer grating metasurface are shown as Supplementary Note 9. In both cases, the VCSEL displays a dominant single emission line that peaks at a wavelength of 855 nm, and a threshold current of 2 mA.

The transmittance of the bilayer grating is measured to be 21%. Although this is lower than that of silicon nanofin polarizers^[30], the measured ER for our bilayer grating is greater than that

of the latter. The transmittance and extinction ratio of the bilayer grating could be boosted by optimizing the fabrication procedure. These could include better planarization of the SU8 substrate, mitigation of charging that occurs during e-beam lithography on the (non-conductive) SU8 layer, and the improvement of the silver film quality. Researchers have fabricated bilayer gratings with extreme ultraviolet (EUV) interference lithography and demonstrated an ER of ~ 6500 times and a transmittance of $\sim 40\%$ at 850 nm ^[27]. Unfortunately, EUV interference lithography is not available to us. Nonetheless, our use of a bilayer grating may inspire other researchers (including those with EUV capabilities) to develop new devices.

We next discuss the polarization control mechanism of our devices. Previous works have utilized differences between the reflection coefficients for TE and TM modes to achieve polarization control. For example, Ostermann et al^[31] made shallow dielectric gratings on the cap of a VCSEL which makes the TE and TM modes have different reflectivity and allows polarization control via the laser feedback effect. In the work we present here, however, the bilayer grating primarily serves as a polarization filter. The operation of the VCSEL is not dramatically affected by the bilayer grating, except that it filters the output light to achieve the desired polarization. We first measure the polarization of the light from the VCSEL before integrating the bilayer polarizer on it. The ratio of the intensity in the long axis of the polarization ellipse to that in its short axis is 8.4 dB at a drive current of 3.19 mA and increases to 11.3 dB for 4.69 mA. Although the ratio varies for different VCSELs, the output is predominantly elliptically polarized. This is mainly caused by the existence of multiple transverse modes. Here we do not oxidize the high aluminum concentration layer $\text{Al}_{(0.98)}\text{GaAs}$ to confine the current, but adopt a method similar to Sato et al^[29], with the extent of the mesa defining the current confinement. This means that multiple transverse modes can lase simultaneously in the cavity since the mesa size exceeds that at which this effect occurs (3-4 μm according to Ref [6]). Fundamental and high order transverse modes usually have different

polarization states (TE or TM). Both the resonator and the gain area of the VCSEL are quasi-isotropic in the plane parallel to the emitting facet, meaning that the VCSEL itself does not have a strong mechanism to select the TE or TM waves. In the device we study here, the only structure with a high degree of linear anisotropy is the bilayer grating, which has much stronger reflectance for TE waves than it does for TM, and much stronger transmittance for TM waves than TE. If the reflectance difference between TE and TM modes were large enough to completely suppress the latter, i.e. if there were a significant laser feedback effect^[31], the output should be TE-only. However, as shown in Figure 5d-e, the output light is polarized along 90° (Design 1) and 0° (Design 2) when the grating wires are along 0° and 90° , respectively. It clearly shows that the output is dominated by TM waves (i.e. light polarized perpendicular to the grating wires), even though TM waves have lower reflectance than TE. This confirms that the laser feedback effect is not the factor that determines the output polarization. We thus conclude that the polarization of the output beam is determined by the anisotropic transmittance of the grating, which blocks TE light and passes TM light.

The bilayer polarizer works well when the illumination is from the bottom substrate side (SU8), as verified above. Similarly, simulations (Supplementary Note 10) predict that when the light impinges on the bilayer polarizer from the air side, the ER and T are basically unchanged. One should thus expect that the device could be used as a polarization sensitive detector when reverse biased. We test this using the set-up shown in the inset of Figure 5f. Light from a laser diode (850 nm wavelength) passes through a polarizer and a half waveplate. By rotating the latter, the polarization direction can be varied. The light transmitted by the half waveplate is loosely focused by a lens onto the VCSEL device at normal incidence. The photocurrent measured as a function of polarization direction is shown in Figure 5f. The peak and dip of the curve correspond to the illuminating beam being TM and TE-polarized, respectively. This confirms that our VCSEL with integrated bilayer grating metasurface can function as a detector

for linear polarization. The measured responsivity of the detector (design 1) for 90°-polarized light is 1.72 mA/W. Detectivity of the device is lower than commonly used photodetectors since only a small portion of the incident light reaches the gain area if we consider the whole resonator structure of the VCSEL (Supplementary Note 11). However, this can be improved by optimizing the structure of the VCSEL. For example, it is reported that a VCSEL with GaAs/AlAs DBR structure and In_{0.2}Ga_{0.8}As single-strained quantum well layer can achieve an absorption of 26% when operating in reverse bias^[32]. The detectivity can also be improved by optimizing the metasurface to increase its transmittance.

It is worth mentioning that although the integrated metasurface transfers the output beam into certain polarization states, the mode stability of the VCSEL used here is not boosted, i. e., the metasurface does not help suppress one particular mode in the cavity. As mentioned in the Introduction part, previously reported polarization control methods are suitable for laser operation, but unsuitable for polarization state detection. Here we could combine the advantages of the two: we could integrate a-si metasurfaces on single mode, polarization stable VCSELs. The polarization detection functions are enabled thereby, and more importantly, the output LCP/RCP beams would have the same wavelength, which is suitable for sensing and data-communication applications. In this paper we demonstrate the generation of CP and linearly polarized light from VCSELs with integrated metasurfaces. However, we note that it should also be possible to generate two arbitrary orthogonally-polarized beams from the VCSEL. This could be done via the method of Mueller et al^[33], but with additional steps. First, we should stabilize the polarization of the light from the VCSEL, e.g. with the bilayer grating we demonstrate in this work. Second, a spacer layer should be formed, e.g. SU8, to serve as a platform to allow another metasurface layer to be added. This metasurface could comprise dielectric nanopillars (e.g. a-Si) with rectangular cross sections. The approach of Mueller et al^[33] could be used to design this metasurface. Each nanopillar can be regarded as a birefringent

wave plate, whose retardance is determined by its geometry (length and width). The fast/slow axes of this waveplate are along the two sides of the rectangular cross section of the nanopillar. It has been shown that a metasurface formed from such nanopillars can decompose an incident beam into two beams of arbitrary orthogonal polarizations that propagate in different directions, with each beam having an independent phase profile^[34]. We anticipate that this capability could open up interesting applications. For example, the two beams could be designed to correspond to images of a three dimensional object from two viewpoints. When combined with additional elements to combine the beams onto a viewing screen and polarization-selective glasses for the user, a stereoscopic image could be viewed ^[35].

3. Conclusion

In conclusion, we have demonstrated two self-contained platforms for the generation and detection of polarized beams. Unlike previously demonstrated VCSEL polarization stabilization methods, the polarization state of the beam is transformed by the integrated metasurface. The output polarization state is thus unmodified even if the VCSEL itself exhibits polarization instability (though the transmitted power may vary). We furthermore demonstrate that our devices can be operated as detectors for circularly (CP) or linearly-polarized light when reverse biased, where the helicity of the CP light, or the x -/ y - polarization direction of the incident light can be distinguished through the photocurrent. The relative simplicity of this approach in terms of fabrication would make these devices amenable for applications for which the polarized emission and/or detection are needed. In addition, we foresee many fruitful opportunities for extending this concept. For example, combining a VCSEL whose output polarization can be electrically switched with a metasurface that generates different beams when illuminated with different polarizations, one could achieve a laser with an electrically reconfigurable output beam.

Supporting Information

Supporting Information is available from the Wiley Online Library or from the author.

Acknowledgements

The authors acknowledge financial support from Australian Research Council under grant number DP180104141. This work was performed in part at the Melbourne Centre for Nanofabrication (MCN) in the Victorian Node of the Australian National Fabrication Facility (ANFF).

Reference

- [1] a) T. Katayama, J. Ito, H. Kawaguchi, *Appl. Phys. Express* **2016**, 9, 072703; b) C. P. McPolin, J.-S. Bouillard, S. Vilain, A. V. Krasavin, W. Dickson, D. O'Connor, G. A. Wurtz, J. Justice, B. Corbett, A. V. Zayats, *Nat. Commun.* **2016**, 7, 1; c) L. Xu, D. Chen, C. A. Curwen, M. Memarian, J. L. Reno, T. Itoh, B. S. Williams, *Optica* **2017**, 4, 468; d) C. Fernandez-Oto, G. De Valcárcel, M. Tlidi, K. Panajotov, K. Staliunas, *Phys. Rev. A* **2014**, 89, 055802.
- [2] a) K. Szczerba, T. Lengyel, M. Karlsson, P. A. Andrekson, A. Larsson, *IEEE Photon. Technol. Lett.* **2016**, 28, 2519; b) A. Liu, P. Wolf, J. A. Lott, D. Bimberg, *Photonics Res.* **2019**, 7, 121.
- [3] E. Prior, C. De Dios, R. Criado, M. Ortsiefer, P. Meissner, P. Acedo, *Opt. Lett.* **2016**, 41, 4083.
- [4] M. Morinaga, X. Gu, K. Shimura, M. Nakahama, A. Matsutani, F. Koyama, presented at 2018 IEEE International Semiconductor Laser Conference (ISLC) **2018**.
- [5] A. Larsson, *IEEE J. Sel. Top. Quantum Electron* **2011**, 17, 1552.
- [6] M. Rainer, *Springer Series in Optical Sciences* **2013**, 166, 560.
- [7] C. M. Long, Z. Mickovic, B. Dwir, A. Caliman, V. Iakovlev, A. Mereuta, A. Sirbu, E. Kapon, *Opt. Express* **2016**, 24, 9715.
- [8] C. Chang-Hasnain, J. Harbison, L. Florez, N. Stoffel, *Electron. Lett.* **1991**, 27, 163.
- [9] G. Verschaffelt, K. Panajotov, J. Albert, B. Nagler, M. Peeters, J. Danckaert, I. Veretennicoff, H. Thienpont, *OPTO-ELECTRON REV.* **2001**, 257.
- [10] G. Verschaffelt, W. Van der Vleuten, M. Creusen, E. Smalbrugge, T. Van de Roer, F. Karouta, R. Srijbos, J. Danckaert, I. Veretennicoff, B. Ryvkin, *IEEE Photon. Technol. Lett.* **2000**, 12, 945.
- [11] a) H. J. Unold, M. Riedl, R. Michalzik, K. J. Ebeling, *Electron. Lett.* **2002**, 38, 77; b) M. C. Huang, Y. Zhou, C. J. Chang-Hasnain, *Nat. Photonics* **2007**, 1, 119; c) T. Mukaihara, N. Ohnoki, Y. Hayashi, N. Hatori, F. Koyama, K. Iga, *IEEE J. Sel. Top. Quantum Electron* **1995**, 1, 667.
- [12] S. Riyopoulos, E. Nhan, *Appl. Phys. Lett.* **2004**, 85, 3038.
- [13] M. Arizleta Arteaga, O. Parriaux, M. Lopez-Amo, H. Thienpont, K. Panajotov, *Appl. Phys. Lett.* **2007**, 90, 121104.
- [14] M. Aljada, K. E. Alameh, Y.-T. Lee, I.-S. Chung, *Opt. Express* **2006**, 14, 6823.
- [15] G. Ortiz, C. Hains, J. Cheng, H. Hou, J. Zolper, *Electron. Lett.* **1996**, 32, 1205.
- [16] D. Louderback, O. Sjolund, E. Hegblom, J. Ko, L. Coldren, *IEEE Photon. Technol. Lett.* **1999**, 11, 304.
- [17] a) Z. e. Bomzon, G. Biener, V. Kleiner, E. Hasman, *Opt. Lett.* **2002**, 27, 1141; b) M. Khorasaninejad, K. B. Crozier, *Nat. Commun.* **2014**, 5, 5386.
- [18] N. F. Yu, Q. J. Wang, C. Pflugl, L. Diehl, F. Capasso, T. Edamura, S. Furuta, M. Yamanishi, H. Kan, *Appl. Phys. Lett.* **2009**, 94.
- [19] Y.-Y. Xie, P.-N. Ni, Q.-H. Wang, Q. Kan, G. Briere, P.-P. Chen, Z.-Z. Zhao, A. Delga, H.-R. Ren, H.-D. Chen, *Nat. Nanotechnol.* **2020**.
- [20] Y. Sun, J. Zhu, S. Liu, Y. Yu, S. Yu, presented at Asia Communications and Photonics Conference **2017**.
- [21] H. Li, D. B. Phillips, X. Wang, Y.-L. D. Ho, L. Chen, X. Zhou, J. Zhu, S. Yu, X. Cai, *Optica* **2015**, 2, 547.
- [22] K. Li, Y. Rao, C. Chase, W. Yang, C. J. Chang-Hasnain, *Optica* **2018**, 5, 10.

- [23] M. S. Seghilani, M. Myara, M. Sellahi, L. Legratiet, I. Sagnes, G. Beaudoin, P. Lalanne, A. Garnache, *Sci. Rep.* **2016**, 6, 38156.
- [24] a) Y. Yang, W. Wang, P. Moitra, I. I. Kravchenko, D. P. Briggs, J. Valentine, *Nano Lett.* **2014**, 14, 1394; b) R. J. Lin, V.-C. Su, S. Wang, M. K. Chen, T. L. Chung, Y. H. Chen, H. Y. Kuo, J.-W. Chen, J. Chen, Y.-T. Huang, *Nat. Nanotechnol.* **2019**, 14, 227; c) A. Arbabi, Y. Horie, M. Bagheri, A. Faraon, *Nat. Nanotechnol.* **2015**, 10, 937; d) S. I. Azzam, K. Chaudhuri, V. M. Shalae, A. Boltasseva, A. V. Kildishev, presented at CLEO: QELS_Fundamental Science **2019**; e) A. I. Kuznetsov, A. E. Miroshnichenko, M. L. Brongersma, Y. S. Kivshar, B. Luk'yanchuk, *Science* **2016**, 354, aag2472; f) L. Jin, Y.-W. Huang, Z. Jin, R. C. Devlin, Z. Dong, S. Mei, M. Jiang, W. T. Chen, Z. Wei, H. Liu, *Nat. Commun.* **2019**, 10, 1; g) S. M. Kamali, E. Arbabi, A. Arbabi, Y. Horie, M. Faraji-Dana, A. Faraon, *Phys. Rev. X* **2017**, 7, 041056; h) H. Sroor, Y.-W. Huang, B. Sephton, D. Naidoo, A. Vallés, V. Ginis, C.-W. Qiu, A. Ambrosio, F. Capasso, A. Forbes, *Nat. Photonics* **2020**, 1.
- [25] a) L. Huang, X. Chen, H. Mühlenbernd, H. Zhang, S. Chen, B. Bai, Q. Tan, G. Jin, K.-W. Cheah, C.-W. Qiu, *Nat. Commun.* **2013**, 4, 1; b) X. Chen, L. Huang, H. Mühlenbernd, G. Li, B. Bai, Q. Tan, G. Jin, C.-W. Qiu, S. Zhang, T. Zentgraf, *Nat. Commun.* **2012**, 3, 1; c) S. Chen, Z. Li, Y. Zhang, H. Cheng, J. Tian, *Adv. Opt. Mater.* **2018**, 6, 1800104; d) X. Li, L. Chen, Y. Li, X. Zhang, M. Pu, Z. Zhao, X. Ma, Y. Wang, M. Hong, X. Luo, *Sci. Adv.* **2016**, 2, e1601102; e) G. Zheng, H. Mühlenbernd, M. Kenney, G. Li, T. Zentgraf, S. Zhang, *Nat. Nanotechnol.* **2015**, 10, 308; f) X. Liu, J. Deng, K. F. Li, M. Jin, Y. Tang, X. Zhang, X. Cheng, H. Wang, L. Wei, G. Li, *Nanophotonics* **2020**, 1.
- [26] N. Yu, P. Genevet, M. A. Kats, F. Aieta, J.-P. Tetienne, F. Capasso, Z. Gaburro, *Science* **2011**, 334, 333.
- [27] Y. Ekinci, H. H. Solak, C. David, H. Sigg, *Opt. Express* **2006**, 14, 2323.
- [28] E. Hecht, *MA: Addison-Wesley Publishing Company* **1998**.
- [29] Y. Sato, K. Furuta, T. Katayama, H. Kawaguchi, *IEEE Photon. Technol. Lett.* **2008**, 20, 1446.
- [30] M. Khorasaninejad, W. Zhu, K. Crozier, *Optica* **2015**, 2, 376.
- [31] J. M. Ostermann, P. Debernardi, C. Jalics, A. Kroner, M. C. Riedl, R. Michalzik, *Opt. Commun.* **2005**, 246, 511.
- [32] H. Kosaka, K. Kurihara, M. Sugimoto, K. Kasahara, *Jpn. J. Appl. Phys.* **1991**, 30, L1172.
- [33] J. P. B. Mueller, N. A. Rubin, R. C. Devlin, B. Groever, F. Capasso, *Phys. Rev. Lett.* **2017**, 118.
- [34] R. C. Devlin, A. Ambrosio, N. A. Rubin, J. P. B. Mueller, F. Capasso, *Science* **2017**, 358, 896.
- [35] X. Goh, Y. Zheng, S. Tan, L. Zhang, K. Kumar, C. Qiu, J. Yang, *Nat. Commun.* **2014**, 5, 5361.